ELSEVIER

Freezing-Induced Strains and Pressures in Wet Porous Materials and Especially in Concrete Mortars

Vesa Penttala
Helsinki University of Technology, Department of Civil Engineering, Concrete Technology, Helsinki, Finland

A theory based on thermodynamics will be presented by which the pressure in the pore structure of wet porous materials can be deduced during freezing. The pore structure is partly filled with liquid and inert gases such as air. The theory is based solely on thermodynamic relationships; no knowledge of the real geometry of the pore system or the degree of liquid filling in the void space is needed. The only inputs needed in the theory are relative humidity and temperature measured in the sample chamber during the freezing. The validity of the theory will be compared with the test results of mortar samples frozen and thawed in a low temperature calorimeter. During the cooling from 20 to −70°C and subsequent heating of the sample, the strains, heat capacity, and ice evolution of the samples were measured simultaneously in the calorimeter. Two of the three mortar samples were produced using an air-entraining admixture. ADVANCED CEMENT BASED MATERIALS 1998, 7, 8–19. *© 1998 Elsevier Science Ltd.*

KEY WORDS: Concrete, Freezing, Mortar, Porous materials, Pressure, Strains

Freezing Theories and Models of Porous Materials

The thermodynamic basis of freezing theories in porous materials were laid by the fundamental works of J. Thomson [1], W. Thomson (later Lord Kelvin) [2], and J.W. Gibbs [3]. The freezing point depression of pore water is related to the pore radius by the equation:

$$\ln\left(\frac{T}{T_0}\right) = -\frac{2 \cdot \Delta G \cdot \nu_w}{\Delta h \cdot r} \tag{1}$$

where T (°K) is the temperature of pore liquid, T_0 (°K) is the freezing temperature of bulk liquid at the pressure of 1 bar, ΔG is the interfacial energy change between matrix and frozen liquid and between matrix and liquid during freezing, ν_w is the specific volume of water, Δh is the latent heat of fusion, and r is the pore radius. The other basic equation used in the freezing theories is the equation of capillary condensation, the so-called Kelvin equation or Laplace equation:

$$\ln\left(\frac{p}{p_0}\right) = \frac{\sigma \cdot M_w}{\rho_w \cdot R \cdot T}\left(\frac{1}{r_1} + \frac{1}{r_2}\right) \tag{2}$$

where p_0 is the saturated vapor pressure of bulk liquid, p is the existing vapor pressure over a concave surface, σ is the surface tension of the liquid, M_w is the molecular weight of the liquid, ρ_w is the density of the liquid, R is the gas constant, T is the absolute temperature in Kelvins, and r_1 and r_2 are the radii of curvature of the liquid in the pore. P. Kubelka [4] took into consideration the tension in the pore fluid and derived Gibbs-Thomson equation (eq 1) to the form where ΔG was unity.

The first to apply these equations to concrete paste was T.C. Powers [5,6] together with his coworkers T.L. Brownyard and R.A. Helmuth [7–9]. Powers started his deduction from the physical fact that, during freezing, water expands about 9% and, if the pore structure was water filled over 91%, freezing caused deterioration of the matrix. Later his theory of hydraulic pressure was refined to take into consideration the fact that, during cooling, the water in the largest pores freezes first, and only after the smaller pores have been frozen would the expansion be hindered, causing large hydraulic pressures and subsequent paste destruction.

Powers and coworkers also observed another freezing mechanism: the growth of the bodies of ice in the capillary cavities or air voids by diffusion of water from the nanometer-sized gel pores. However, they assumed that this mechanism also always caused expansion in hardened Portland cement paste. Their experiments showed that empty air voids limit the hydraulic pressure and shorten the period during which ice in the cavities can increase. The closer these entrained air

Address correspondence to: Dr. Vesa Penttala, Department of Civil Engineering, Concrete Technology, Helsinki University of Technology, Rakentajanaukio 4A, FIN-02150 Espoo, Finland.
Received December 9, 1996; Accepted April 23, 1997

© 1998 by Elsevier Science Ltd.
655 Avenue of the Americas, New York, NY 10010
ISSN 1065-7355/98/$19.00
PII S1065-7355(97)00011-4

voids are to each other, the more effective they are in controlling the two freezing mechanisms. They also noticed the effects of the freezing rates. At a low freezing rate the diffusion of gel water is the dominant feature causing drying shrinkage in the gel structure, whereas at a fast freezing rate diffusion of the gel water does not have time to evolve and hydraulic pressure governs the freezing deterioration and induces cracks in the matrix. They were also able to show that osmotic pressures have a role in freezing of cement paste, especially when considerable amounts of salts are present in the pore liquid.

Based on thermodynamics, the generalized Gibbs-Thomson equation (eq 1), and Laplace's equation (eq 2), D.H. Everett and J.M. Haynes [10,11] showed that ice in a larger pore could expand or grow to a smaller, water-filled pore only when the interface between the ice and water in the connecting tube between the large and smaller pores was curved. Due to this curvature a lower pressure would be induced in the smaller, unfrozen pore water, which would draw water from the smaller pores to the ice crystal until ice could not expand further because of lack of space.

The third important theoretical impact on the freezing theories of porous solids was provided by G. Litvan [12–15]. According to Litvan's model, the surface forces of pores have an important effect during the freezing of pore liquid. These surface forces hinder ice crystal formation, and the water layer situated a few molecular diameters from the surface remains structurally oriented during the freezing of the rest of the pore water. According to Litvan, the vapor pressure of these metastable, undercooled structural water layers exceeds the vapor pressure of the solid phases of ice and matrix, causing moisture transport from the pores to the outer surface of the test sample. Similarly, according to Litvan, if the cooling rate of the sample is faster than the rate of the transport process, freezing damage occurs.

M.J. Setzer [16] criticizes Litvan's assumptions of constant surface stresses in the adsorbed interface between vapor and the capillary condensed liquid, where Litvan assumes a zero contact angle between the liquid meniscus and pore surface. According to Litvan's simplified assumptions, for example, gel water could not freeze. Setzer presented a revised thermodynamic model based on Litvan's basic assumptions but took into consideration the changes in surface stresses in the adsorbed water layer on the pore surface during the thickness changes of this adsorbed, structurally oriented water layer. This structurally oriented, superficial water layer freezes only at very low temperatures from −90 to −100°C. In his presentation Setzer is the first to derive an approximate equation for the pressures induced in a totally water-filled porous material during freezing. According to Setzer, if the liquid is water, the pressure difference induced by freezing is:

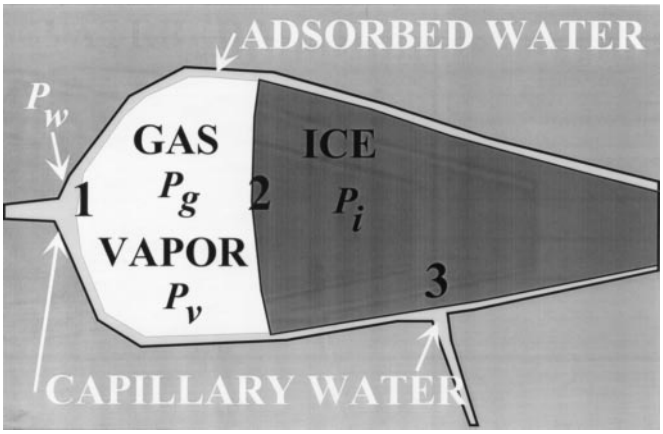

FIGURE 1. Conceptual drawing of a situation in a freezing pore. Numbers 1, 2, and 3 denote different freezing conditions.

$$\Delta p = 1.22 \cdot (T_0 - T) \tag{3}$$

where Δp is in MPa, T is the freezing temperature of the pore water in Kelvins, and $T_0 = 273.15$°K is the freezing temperature of bulk water. This linear relationship is of a highly approximate nature because of the rather crude assumptions Setzer made regarding the coefficient of surface tension, which has been assumed to be a constant although it really is a function of pore size.

The Theory

The thermodynamic state in a pore of the material presented in Figure 1 will be studied. The chemical potentials of ice, adsorbed or capillary water, and some inert gas (for example, air) will be discussed. It has been shown by Brun and coworkers [17] that the Gibbs-Duhem equations, which govern the freezing phenomenon of highly dispersed liquid in porous materials in which gas phases are also present, cannot be solved in closed form except in a particular case where the solid-gas interphase is plane. However, this situation in which all of the pores are totally filled with water is, in this author's opinion, unrealistic in almost all practical cases of concrete structures. For example, when a test specimen is taken out of water immersion to a relative humidity of <100%, a large portion of the largest pores having dimensions >10 μm are emptied of water and filled with gas and water vapor. Similarly, concretes that have been produced using large amounts of binders dry inside, even under water, due to the self-desiccation caused by the hydration process, which can lower the relative humidity in the pore structure to

75%. The situation presented in Figure 1 will prevail, especially in the larger pore dimensions. During the freezing process, even water from gel pores having diameter around 2 nm will be diffused to ice situated in larger pores, causing shrinkage of the matrix and the introduction of gas voids to the pore spaces.

To derive a theoretical solution to the problem of freezing in a porous solid in which gas phases are also present in the pore structure, some simplifying assumptions have to be made. In the deduction of the presented theory, the surface forces acting between the pore surface and pore water have been neglected.

The derivation of the theory will be done for water; all other liquids can be handled similarly. During the equilibrium situation at the freezing temperature, T, the chemical potentials of ice, μ_i, must be equal to the chemical potential of water, μ_w:

$$\mu_i(T, p) = \mu_w(T, p) \tag{4}$$

where p is the pressure in the pore void. Similarly, the chemical potential of water vapor must also be in equilibrium with water and ice.

If water vapor is considered as an ideal gas:

$$\mu_v(T, p) = \mu_v(T, p_0) + R \cdot T \cdot \ln\left(\frac{p_v}{p_0}\right) \tag{5}$$

where $p_0 = 1$ bar $= 0.1$ MPa, a reference pressure. For liquids and solids the chemical potential has the form:

$$\mu_w(T, p) = \mu_w(T, p_0) + \nu_w(T) \cdot (p - p_0) \tag{6}$$

$$\mu_i(T, p) = \mu_i(T, p_0) + \nu_i(T) \cdot (p - p_0) \tag{7}$$

where ν_w and ν_i are the molar volumes of water and ice, respectively. Terms $\mu_v(T, p_0)$, $\mu_w(T, p_0)$, and $\mu_i(T, p_0)$, can be presented as:

$$\mu_v(T, p_0) = \mu_v^\circ(T_0) + \int_{T_0}^{T} \frac{\partial \mu_v^\circ}{\partial T}\, dT$$

$$= \mu_v^\circ(T_0) + \int_{T_0}^{T} (-s_v^\circ(T))dT \tag{8}$$

$$\mu_w(T, p_0) = \mu_w^\circ(T_0) + \int_{T_0}^{T} \frac{\partial \mu_w^\circ}{\partial T}\, dT$$

$$= \mu_w^\circ(T_0) + \int_{T_0}^{T} (-s_w^\circ(T))dT \tag{9}$$

$$\mu_i(T, p_0) = \mu_i^\circ(T_0) + \int_{T_0}^{T} \frac{\partial \mu_i^\circ}{\partial T}\, dT$$

$$= \mu_i^\circ(T_0) + \int_{T_0}^{T} (-s_i^\circ(T))dT. \tag{10}$$

Specific entropy in eqs 8–10 can be calculated from:

$$s^\circ(T) = s^\circ(T_0) + \int_{T_0}^{T} \frac{\partial s^\circ(T_0)}{\partial T}\, dT$$

$$= s^\circ(T_0) + \int_{T_0}^{T} \frac{c_p^\circ}{T}\, dT. \tag{11}$$

The specific heat capacities of water vapor, water, and ice cannot be considered constant in the rather large temperature range in question and, therefore, the following equations were used [17]:

$$c_{pi}^\circ(T) = 38.052 \cdot [1 + 373.7 \cdot 10^{-5} \cdot (T - T_0)] \tag{12}$$

$$c_{pw}^\circ(T) = 75.996 \cdot [1 - 54.0 \cdot 10^{-5} \cdot (T - T_0)]. \tag{13}$$

The specific heat capacities of eqs 12 and 13 are presented in J/mol.

In a wet pore there are three different principal freezing situations that are represented by numbers 1, 2, and 3 in Figure 1. Point 1 represents the situation of unfrozen capillary water. The same freezing situation exists when pore water first freezes. The solution equation is obtained by substituting eqs 6, 7, and 9–11 into the equilibrium equation (eq 4). The following equation is obtained:

$$\mu_w^\circ(T_0) - s_w^\circ(T_0) \cdot (T - T_0) - \int_{T_0}^{T}\int_{T_0}^{T} \frac{c_{pw}^\circ}{T}\, dTdT + \nu_w(T) \cdot (p - p_0) = \mu_i^\circ(T_0) - s_i^\circ(T_0) \cdot (T - T_0) - \int_{T_0}^{T}\int_{T_0}^{T} \frac{c_{pi}^\circ}{T}\, dTdT + \nu_i(T) \cdot (p - p_0). \tag{14}$$

In an equilibrium state at point 1 when a gas phase and liquid phase are in contact with each other, the chemical potential of water vapor equals the chemical potential of the same component in the liquid phase:

$$\mu_w(liquid) = \mu_v(gas). \tag{15}$$

Applying the relation shown in eq 15 to eqs 5 and 6 gives the following equation:

$$\nu_w(T) \cdot (p - p_0) = R \cdot T \cdot \ln\left(\frac{p_\nu}{p_0}\right) \tag{16}$$

which can be placed into eq 14. At the reference temperature $T_0 = 273.15$°K and pressure $p_0 = 1$ bar, water and ice are in equilibrium:

$$\mu_w^\circ(T_0) = \mu_i^\circ(T_0)$$

that is,

$$h_w^\circ(T_0) - T_0 \cdot s_w^\circ(T_0) = h_i^\circ(T_0) - T_0 \cdot s_i^\circ(T_0)$$

and

$$s_w^\circ(T_0) - s_i^\circ(T_0) = \frac{h_w^\circ(T_0) - h_i^\circ(T_0)}{T_0} = \frac{\Delta h_{wi}^\circ}{T_0} \tag{17}$$

where Δh_{wi}° is the freezing heat of the water at 273.15°K. Introducing eq 17 into eq 14, the solution equation for this freezing situation is achieved:

$$p - p_0 = \frac{R \cdot T}{\nu_i} \cdot \ln\left(\frac{p_\nu}{p_0}\right) + \frac{\Delta h_{wi}^\circ}{\nu_i \cdot T_0}(T_0 - T) + \frac{1}{\nu_i} \cdot \int_{T_0}^{T} \int_{T_0}^{T} \frac{c_{pi}^\circ - c_{pw}^\circ}{T} dT dT \tag{18}$$

in which the reference pressure $p_0 = 0.1$ MPa and reference temperature $T_0 = 273.15$°K. If the pore liquid is water, the specific volume of ice $\nu_i = 1.998 \cdot 10^{-5}$ m^3/mol and $\Delta h_{wi}^\circ = 6.0 \cdot 10^3$ J/mol. The gas constant, R, is 8.314 J/mol/K.

Using similar deduction for freezing situation 2, in which ice is forming on the surface between water vapor and ice, the following equation can be derived:

$$p - p_0 = \frac{R \cdot T}{\nu_i} \cdot \ln\left(\frac{p_\nu}{p_0}\right) + \frac{\Delta h_{vi}^\circ}{\nu_i \cdot T_0}(T_0 - T) + \frac{1}{\nu_i} \cdot \int_{T_0}^{T} \int_{T_0}^{T} \frac{c_{pi}^\circ - c_{pv}^\circ}{T} dT dT \tag{19}$$

in which Δh_{vi}° is the sublimation heat of the vapor to solid. For water, $\Delta h_{vi}^\circ = 51.0 \cdot 10^3$ J/mol. The freezing equation at point 3 in Figure 1 gets the form:

$$p - p_0 = \frac{\Delta h_{wi}^\circ}{(\nu_i - \nu_w) \cdot T_0}(T_0 - T) + \frac{1}{(\nu_i - \nu_w)} \cdot \int_{T_0}^{T} \int_{T_0}^{T} \frac{c_{pi}^\circ - c_{pw}^\circ}{T} dT dT. \tag{20}$$

If the pore liquid is water, the specific volume is $\nu_w = 1.8 \cdot 10^{-5}$ m^3/mol.

Comparing freezing eqs 18–20 it can be noted that eqs 19 and 20 cause approximately 10 times larger freezing pressures in the pore structure compared to eq 18. Freezing equation 18 is energetically most advantageous and, therefore, it governs the freezing process of wet porous solids. During the freezing process of porous solids, when freezing has commenced in so small pore sizes that they are totally filled with liquid before freezing, only then does eq 20 become valid.

In an equilibrium state when a gas phase and liquid phase are in contact with each other, the chemical potential of water vapor equals the chemical potential of the same component in the liquid phase according to equation 15. The chemical potential of water vapor in the pore spaces inside the continuously porous material can be calculated merely by measuring the partial water vapor pressure in the test chamber outside the test sample. When this assumption is used, the surface forces acting between the pore surface and pore water have been neglected. When freezing commences in the smallest pores, equation 15 can no longer correctly convey the information of the pressures in the pore system to the outside chamber in the form of vapor pressure. This will govern the applicability range of the presented theory.

When the pressure in the test chamber is the same as the reference pressure, $p_0 = 0.1$ MPa, p_ν/p_0 equals the relative vapor pressure, φ, in the test chamber. This can be measured and inserted into eq 18. The pressure of the inert gas in the chamber has a marginal effect on the vapor [18].

In eqs 18–20, p denotes the pressure in the pore space, and eq 18 enables the calculation of pressure in the pore system during freezing by merely measuring the relative vapor pressure in the test chamber as a function of temperature, T. It must be emphasized that eq 18 is valid only after ice is present in the pore system. If the pore system was totally free of gas bubbles and all the pores were filled with water, eq 20 would govern the freezing process. In this situation the freezing pressure in the porous solid would increase remarkably compared to the situation studied in this article.

Tests with Mortars

Three mortar samples were produced to validate the presented theory. The composition of the mortars was chosen to represent the ingredients of normal concretes in which the larger aggregate fractions from 2 to 16 mm have been omitted. This explains the large binder amounts of the test mortars presented in Table 1. Test mortar M50 was a normal mortar in which no air-entraining admixtures were used, whereas in test mor-

TABLE 1. Composition and compressive strength results of the test mortars

Test Mortar	M50	M60A	M35A
Aggregates (kg/m^3) total	1155	1004	1266
1–2 mm	266	231	291
0.5–1.2 mm	266	231	291
0.1–0.6 mm	346	301	380
<0.125 mm	277	241	304
Cement (kg/m^3)	583	656.6	393.7
Water (kg/m^3)	340	262.6	231.7
Air-entraining admixture (kg/m^3)	—	1.31	1.95
Compressive strength (MPa) 100-mm cubes	50.7	59.5	34.6

tars M60A and M35A extra air was introduced into the mix with an air-entraining agent. Test mortar M35A was run with a test arrangement in which the temperature of the sample chamber was measured, whereas in the two other mortar cases only the block temperature of the calorimeter could be measured. The first test arrangement was much more complicated because the wires of the temperature gauge had to be installed in the small sample chamber in addition to the wires of the two strain gauges and the relative humidity measuring device. However, this test arrangement provided results in which the temperature changes due to heat release during freezing could be detected. Because of data transfer problems, the computer measuring strain, temperature, and relative humidity data of test mortar M35A booted twice during the run, and, therefore, the test curves in Figures 5, 9, and 10 are incomplete.

The binder used was rapid hardening Portland cement CEM52,5R of local origin produced by Finnsementti Oy (Table 2). The aggregates were sieved into five fractions and their petrographic composition was mostly granite. The air-entraining admixture was a vinsol resin.

TABLE 2. Chemical composition and physical properties of the cement CEM52,5R

Chemical Composition (w-%)	CEM52,5R
CaO	62.3
SiO_2	20.3
Al_2O_3	4.5
Fe_2O_3	2.9
MgO	3.9
K_2O	0.84
Na_2O	0.92
SO_3	3.2
Loss of ignition (950°C)	0.8
Physical Properties	
Compressive strength (MPa)	
1 d	31.2
7 d	48.8
28 d	56.9
Specific area (Blaine) (m^2/kg)	446

TABLE 3. Measured weights of the wet duplicate test prisms during the different test phases and the air content of the fresh mortar paste measured by the pressure test

Test Concrete	Weight in Water (g)	Weight in Air at the Beginning of the Test (g)	Dry Weight (g)	Air Content (%)
M50	7.44	13.28	11.39	0.8
M60A	7.34	13.43	11.48	6.5
M35A	5.98	11.64	9.04	8.4

After mixing for 4 minutes the test mortars were poured into 2-dl polyethylene bottles, which were rotated for 5 hours to prevent segregation. At the age of 3 days the bottles were cut open and $10 \cdot 10 \cdot 55$ mm^3 prisms were cut. Two strain gauges were glued on opposite sides of one of the prisms. The prism was placed into a desiccator in vacuum for 2 days; thereafter, it was immersed in water for 5 days. A comparison prism was oven-dried at 105°C for 1 week after it was cut. At the age of 35 days two strain gauges were glued on the dry comparison sample and wires were soldered to the strain gauges. It was then placed into the reference chamber of a low temperature calorimeter. At the same time, the wet sample was taken from the water, wires were similarly soldered to the strain gauges, and the sample was placed in the other measuring cell of the calorimeter. The wiring procedure of the wet sample lasted from 7 to 10 minutes; during this time a considerable amount of water evaporated from the mortar prism. The evaporated and retained water amounts were measured by weighing a duplicate wet sample at the consequent time intervals and by drying the duplicate sample later in oven (Table 3). The pore size distributions of the test mortars are presented in Figure 2.

During the cooling test the strains of the wet and dry samples were measured every 40 seconds. The strain gauges were calibrated using steel samples for which the coefficient of temperature expansion was known. At the same time intervals, the relative humidity in the test chambers was measured by special humidity gauges produced by Vaisala Oy. The difference in the heat capacities of the wet and dry test samples was measured by the low temperature calorimeter produced by Setaram. The cooling rate of the test was 3°C/hour and the following heating rate was 4.4°C/hour. The test started from +20°C and the temperature dropped linearly to −70°C and again increased back to +20°C after a few hours at −70°C.

The strain results of the test samples are presented in

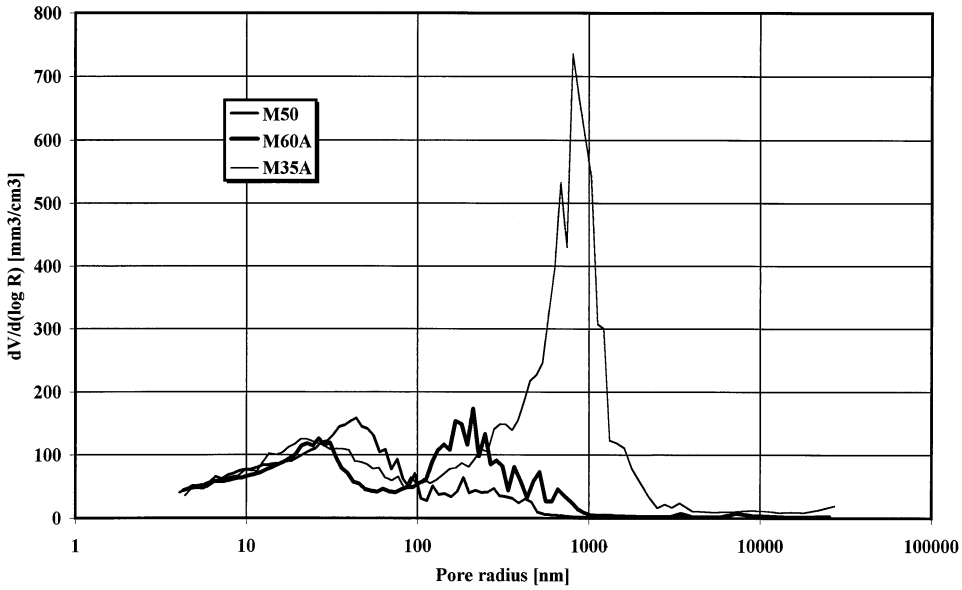

FIGURE 2. Pore size distribution of the test mortars produced by mercury intrusion porosimetry. Sample preparation and testing procedures are similar to those in reference 19.

early to −70°C and again increased back to +20°C after a few giyrs at −70°C.

The strain results of the test samples are presented in Figures 3–5. Heat capacities of the wet test mortars and the formed ice amounts are presented in Figures 6–8. The relative humidity measurements in the test chamber of the wet samples are shown in Figure 9, and the pressure results calculated according to eq 18 are presented in Figure 10. In Figures 11–13 the freezing strain results of test mortars M50 and M35A are compared to theoretical results obtained by superposing the strains caused by the freezing pressures presented in Figure 10 to the strains of the dry test specimens. The shrinkage strains caused by water movement in the porous solid during the freezing process have not been taken into consideration.

Discussion

As the dilation curves of Figures 3–5 show, test specimens M50 and M60A exhibit a large expansion when the water in the largest pores of the mortar prisms first freezes. Air-entrained lower strength test specimen M35A also expands during the first freezing, but the expansion is much smaller compared to the two other mortars. It can also be noted that the remaining dilations after the freezing and thawing test were quite large for M50 and M60A mortars ($3.6 \cdot 10^{-4}$ and $1.6 \cdot$

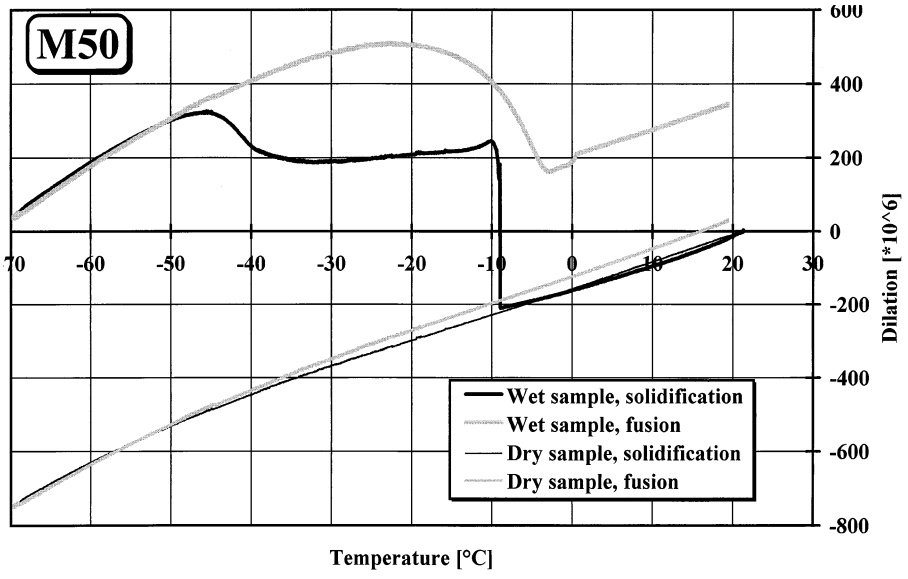

FIGURE 3. Dilations of the test prisms of mortar M50.

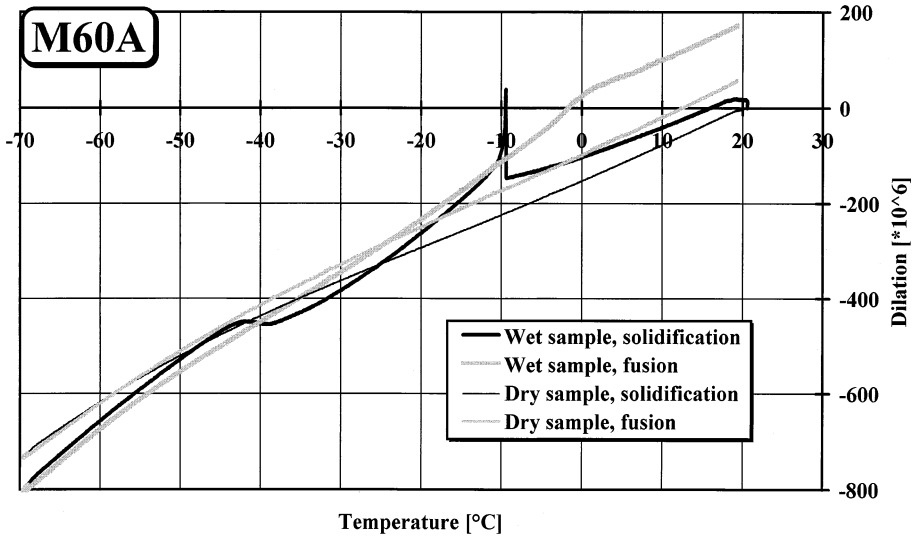

FIGURE 4. Dilations of the test prisms of mortar M60A.

10^{-4}, respectively). The dry test specimens M50 and M60A also exhibit noteworthy remaining expansions after the test ($0.5 \cdot 10^{-4}$ and $0.6 \cdot 10^{-4}$, respectively). The remaining dilations of test mortar M35A were much smaller ($0.3 \cdot 10^{-4}$ and $0.25 \cdot 10^{-4}$ for wet and dry samples, respectively).

The large remaining dilations after the freezing and thawing test of test mortars M50 and M60A indicate that remarkable specimen cracking has occurred during the test. On the other hand, the remaining dilation in the air-entrained low strength test mortar M35A was very near the remaining dilation of the dry comparison sample. It shows that no significant cracking has occurred due to freezing or thawing of the pore water.

The calculation of the freezing stresses caused by the expansion of the test prisms during the first freezing indicates that test mortar M50 should possess 17.0 MPa tensional strength if no cracking is induced in the test prism. The respective values for M60A and M35A are 7.3 and 1.8 MPa. Previous investigations of the tensional properties of concrete and mortar [20] imply that the direct tensional strengths of the test mortars M50, M60A, and M35A are approximately 3.7, 3.9, and 2.9 MPa, respectively. The tensional capacity of only M35A exceeds the stresses that are induced into the test prisms during the first freezing. In the microscopy investigation, cracks were detected in tests mortars M50 and M60A after the test. In test mortar M35A, cracks were not seen in the outer surface of the wet test prism after the freezing and thawing test.

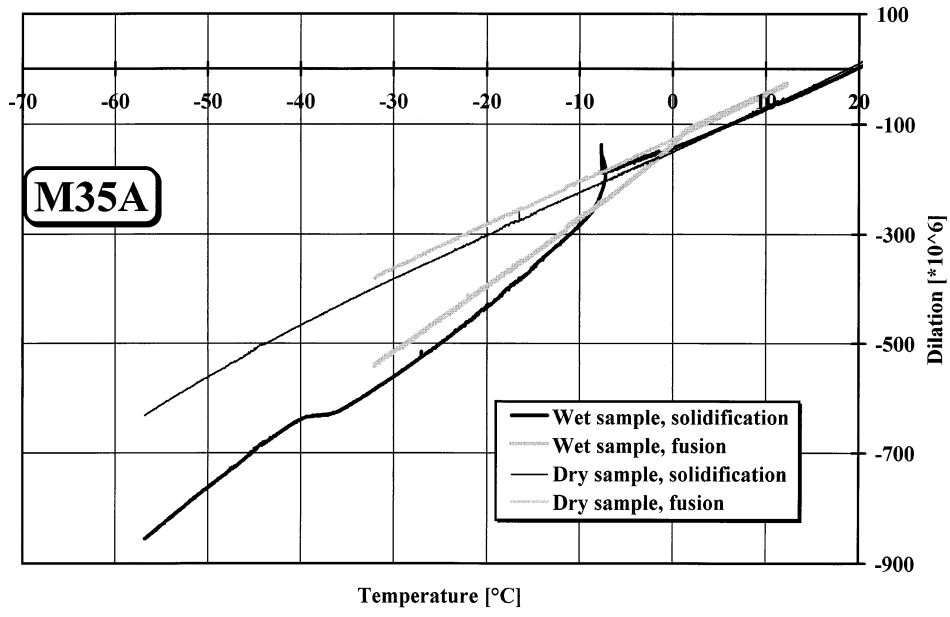

FIGURE 5. Dilations of the test prisms of mortar M35A.

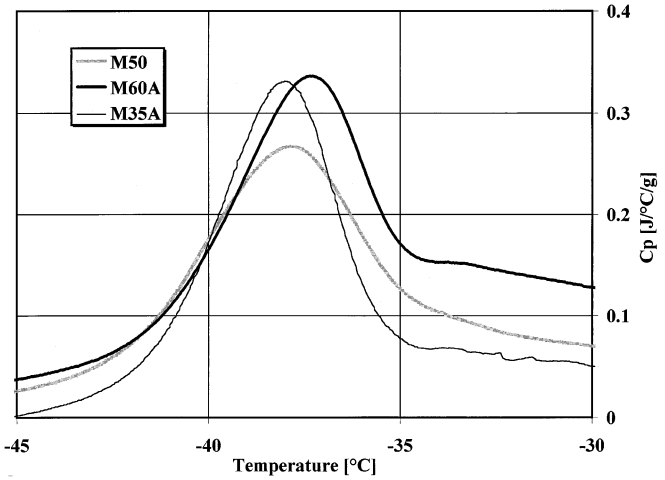

FIGURE 6. Heat capacity differences of the wet and dry test samples of the three mortars in the temperature range at which water in the gel pores freezes.

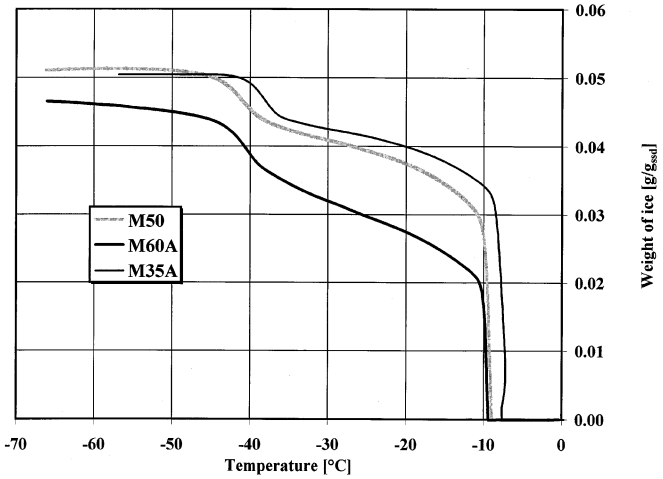

FIGURE 8. Ice evolution of the test mortars in g/g of the saturated surface dry specimens.

The pressures at the temperature when first freezing of pore water occurred and calculated by eq 18 and presented in Figure 10 would cause tensional stress values of 13.4, 3.2, and 1.8 MPa for test mortars M50, M60A, and M35A, respectively. These pressure values would cause the strains in the test prisms presented in Table 4.

The results listed in Table 4 show that the test results of M50 and M60A exceed the expansion values obtained by eq 18, whereas the theoretical and test values of M35A are quite near each other. This is in line with the previous reasoning of cracking in the test specimens.

The behavior of the test prisms below the first freezing temperature is totally different for mortar M50, in which no air-entraining agents were used, and the air-entrained mortars M60A and M35A. During the temperature decrease after the first freezing expansion, the wet mortar prism M50 expands compared to the dilation of the dry comparison sample. In the air-entrained mortars M60A and M35A, the situation is quite opposite. The wet mortar prisms contract rapidly after the expansion and only when the gel water begins to freeze below −35°C is another expansion noted in the test prisms.

The reason for the rapid contraction after the first expansion of mortars M60A and M35A can be seen in Figure 10. The pressure in the pore system of the air-entrained mortars changes sign from over pressure to under pressure, which is the reason for the rapid contraction. The contraction takes place in test mortar M60A even though it has cracked during the first

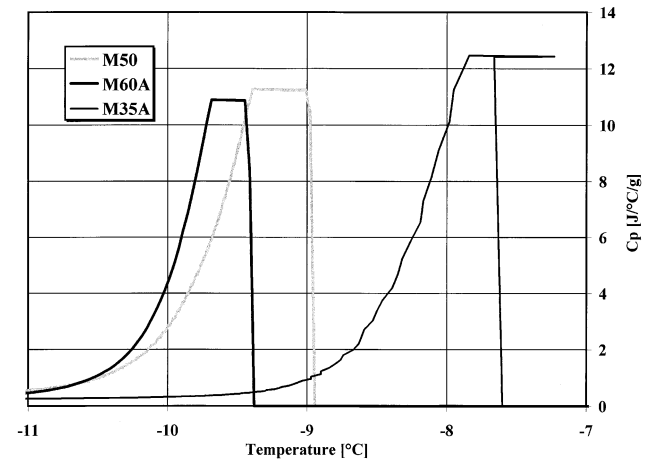

FIGURE 7. Heat capacity differences of the wet and dry test samples of the test mortars when the first ice formation takes place. The curves of test mortars M50 and M60A were produced by using the block temperature of the calorimeter, whereas in test mortar M35A the temperature was measured from the test chamber.

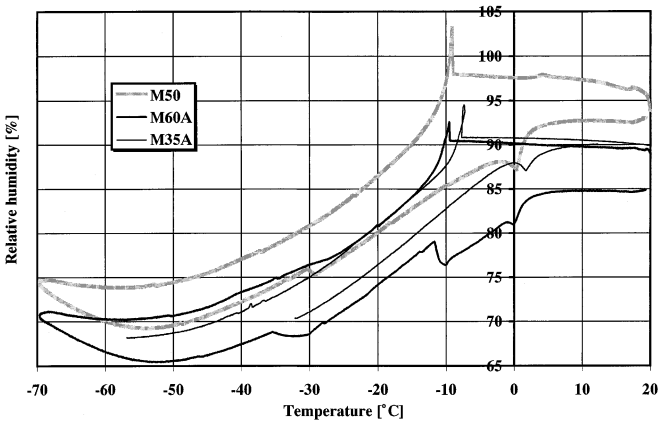

FIGURE 9. Relative humidity in the calorimeter chamber of the wet test mortars during the cooling and heating run.

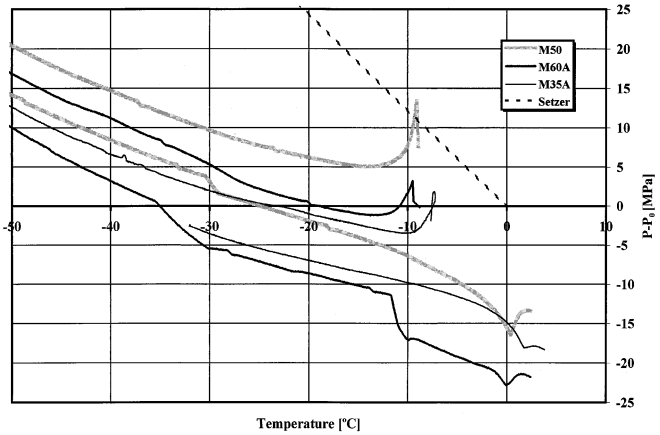

FIGURE 10. Pore pressures in the wet test mortars according to eq 18.

expansion. The thermodynamic reason is already presented in the literature survey portion of this article by Everett and Haynes [10,11]. Ice that forms in the larger pores draws unfrozen water from the smaller pores due to the lower chemical potential at the ice surface compared to the unfrozen water. This suction causes lowering of the pore pressure. The low pressure phase in the pore system of M35A goes down to −25°C, and for M60A this lasted down to −19°C.

The suction of gel water from the smaller pores, which have a large surface area, causes inevitable shrinkage of the matrix, and this increases the contraction of the air-entrained mortars during the temperature decrease. The intention of the author was not to calculate or deduce the theory of shrinkage during freezing. However, the test results seem to give credit to the presented thermodynamic freezing pressure theory.

The relative humidity in the calorimeter chamber of the wet mortars is presented in Figure 9. When the first freezing of the pore water takes place, the expanding pressure in the pore system drives water out of the test sample and the relative humidity in the chamber is abruptly increased. When ice forms in the pore system, this draws water vapor back from the chamber and the relative humidity of the chamber decreases.

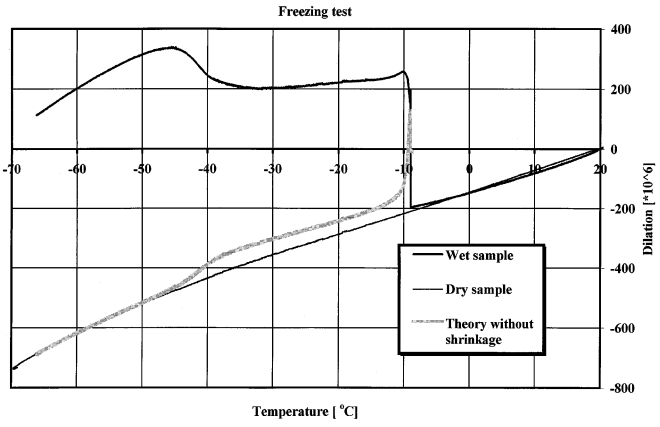

FIGURE 11. Theoretical and measured freezing strains of test mortar M50. In the theory, the strains caused by the shrinkage of the colloidal gel due to water movement during the freezing process are not taken into consideration.

Two evolution maxima are presented in the heat capacity curves of Figures 6 and 7. The first freezing of M35A, which possesses the largest capillary pores of the test mortars, takes place at a temperature of −7.7°C. M50 freezes at −8.9°C and M60A at −9.4°C. The curve of M35A is made by using the chamber temperature, whereas the two other test curves are produced by using the block temperature of the calorimeter. In the curves of M35A shown in Figures 7 and 8, the warming effect of heat liberated during the first ice formation can be seen. This causes the chamber temperature to increase by nearly 0.5°C. The same phenomenon can be seen in the freezing dilation curve of Figure 13. The other smaller heat capacity evolution maximum is noted in Figure 6 around the −35 to −40°C temperature range. In this temperature range, a portion of gel water that is situated in voids having a dimension of 2 to 4 nm is frozen.

To evaluate the effect of shrinkage-induced contraction in the air-entrained test mortars, the dilations caused by the pore pressures of eq 18 were calculated theoretically and compared to the test results of test mortars M50 and M35A (Figures 11–13). When the first freezing takes place, the pore pressure is effective on the whole cross-section of the prism. When part of the pore water is transformed into ice, the pore pressure no longer has an effect on the whole cross-section, and the pressure area is diminished in relation to the amount of unfrozen water in the pore system. The dilation caused by the pore pressure presented by eq 18 can be superposed on the dilation of the dry test prism according to equation:

$$\epsilon_{wet}(T) = \epsilon_{dry}(T) + \frac{p - p_0}{E_{con} + E_{ice} \cdot V_{ice}(T)/V_{tot}} \cdot \frac{\Sigma m_{ice} - m_{ice}(T)}{\Sigma m_{ice}} \quad (21)$$

where

$$E_{con} = 5000 \cdot \sqrt{f_c}\ \text{(MPa)}$$

and

$$E_{ice} = [5.69 - 0.0648 \cdot (T - 273.15)] \cdot 1425\ \text{(MPa)}$$

where f_c is compressive strength of concrete in (MPa), Σm_{ice} is the total ice amount in the pore system of the

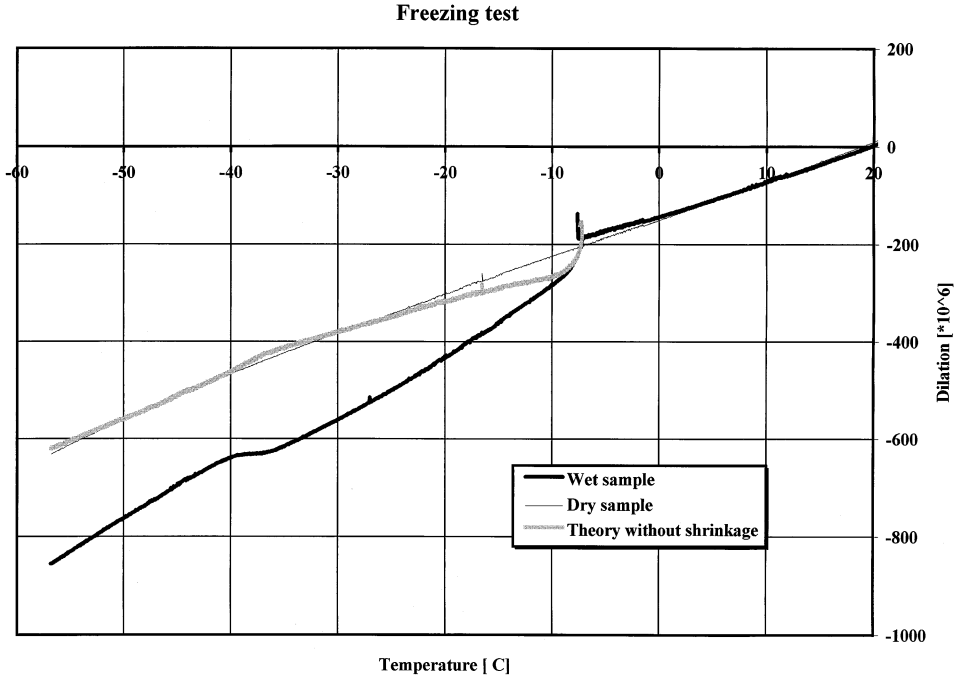

FIGURE 12. Theoretical and measured freezing strains of test mortar M35A. In the theory, the strains caused by the shrinkage of the colloidal gel due to water movement during the freezing process are not taken into consideration.

sample at −70°C, and $m_{ice}(T)$ is the ice amount in the sample at the temperature under consideration.

Equation 21 is based on the theory of linear elasticity in which no cracks are assumed to be induced into the structure. The formula for the modulus of elasticity of ice, E_{ice}, is combined from the publications of P.V. Hobbs [21] and I. Hawkes and M. Mellor [22]. The theoretical dilation curve of test mortar M50, in which no air-entraining admixtures were used, is presented in Figure 11. Because the pore pressure after the first expansion decreases abruptly, as presented in Figure 10, the theoretical dilation also contracts. However, in reality, the prism is severely cracked and as the pore pressure of M50 does not change its sign, the prism stays in its extended length. The form of the dilation curve below the first freezing temperature is similar to

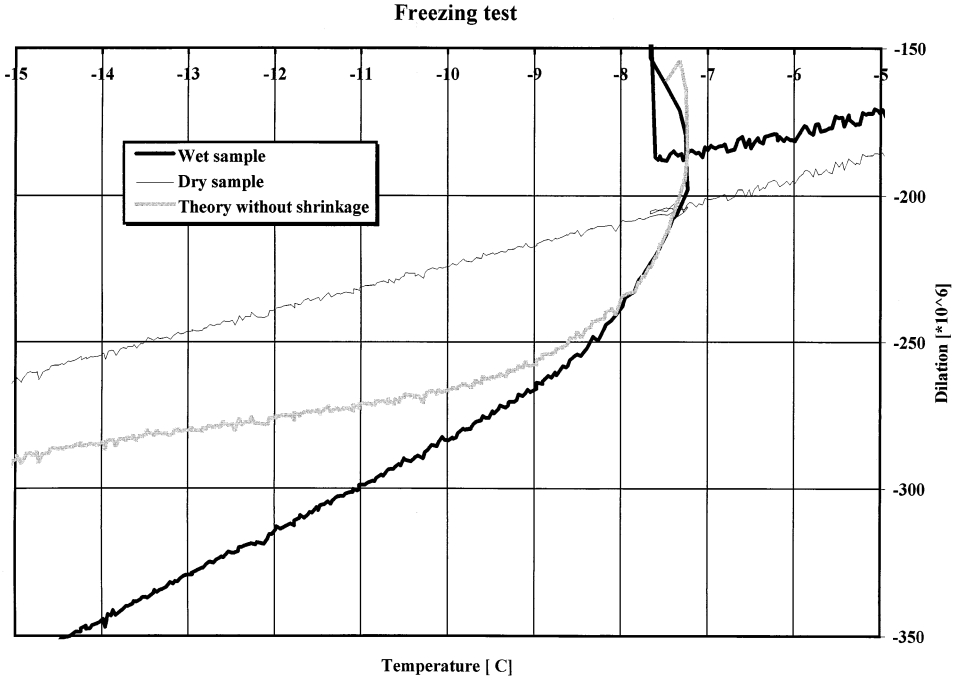

FIGURE 13. Theoretical and measured freezing strains of test mortar M35A when ice evolution is first detected. In the theory, the strains caused by the shrinkage of the colloidal gel due to water movement during the freezing process are not taken into consideration.

TABLE 4. Measured and theoretical expansion dilations of the test mortar prisms at the temperature of the first freezing

Test Mortar	Expansion (10^4)	
	Test Result	Eq 18
M50	4.5	3.6
M60A	1.9	0.8
M35A	0.5	0.6

that of the theoretical curve, but it is somewhat more pronounced. This is most likely because, at low temperatures, freezing takes place in small pores that do not contain water vapor and gas, and freezing pressures are governed by eq 20 instead of eq 18. Therefore, the freezing pressures are much higher. The change from eq 18 to eq 20 takes place gradually, and no abrupt jump in the pore pressure is noted.

In Figure 13 the theoretical and measured freezing strains of test mortar M35A follow each other very precisely in the beginning of the freezing. When temperature decreases 1.5°C from the first freezing temperature shrinkage dilations start to govern the freezing strains and they form the major portion of the difference between the dilations of dry and wet mortar samples, as can be noted in Figure 12.

When the thawing dilations of the test mortars are studied in Figures 3–5, it can be noted that only test mortar M50 shows a major hysteresis behavior. The thawing dilation of M50 starts to deviate from a straight line only after the temperature has risen to about −25°C. This is approximately the same temperature at which the pore pressure changes its sign during thawing, shown in Figure 10.

In the air-entrained test mortars the thawing dilation curve is straighter compared to the freezing dilation curve, and the thawing curve forms an angle from nearly a straight line only after almost all ice has melted near 0°C.

Range of Applicability of the Theory

When freezing commences in the smallest pores, eq 15 can no longer correctly convey information regarding the pressures in the pore system to the outside chamber in the form of vapor pressure. When the pore pressures shown in Figure 10 are compared to the dilations of the test mortars shown in Figures 3–5 one can note that the under pressure in the air-entrained mortars M60A and M35A prevails down to −19°C and −25°C, respectively. According to the dilation results, the contraction of these mortars increases down to −30 . . . −35°C and, therefore, the applicability range of the solution eq 18 could not extend below −20°C, possibly not even below −15°C. This corresponds to the freezing of pores having a diameter of about 10 nm. With such a limited applicability range, the last integral term in eq 18 has only a small effect on the pore pressure and it can be omitted. At −15°C its effect is <5%.

Conclusions

1. A theory based on thermodynamics was derived by which the pressure in the pore system of a porous body can be calculated during freezing by merely measuring the relative humidity in the test chamber as a function of temperature. The applicability range of the theory is estimated not to extend below −15 . . . −20°C.
2. Saturated, surface dry mortars expand during the first freezing irrespective of the air-entrainment.
3. Use of air-entraining admixtures decreases the expansion at the temperature at which the first freezing of pore water takes place. Even a 6.5% air-entrainment in mortar does not necessarily hinder the cracking of mortar during the first freezing.
4. The dilations of air-entrained and normal mortars in which no air-entraining admixtures have been applied differ completely from each other below the temperature at which the first freezing of pore water takes place. Wet mortars without air-entrainment continue to expand compared to dry comparison mortars when temperature is decreased. Wet air-entrained mortars contract abruptly after the expansion of the first freezing. This is due to the under pressure in the pore system caused by the suction of water from the smaller pores to the ice surfaces in the larger pores. As the temperature is decreased, shrinkage caused by the water transfer from gel structure also contributes increasingly to the contraction dilations in air-entrained mortars.
5. When the first freezing of the pore water in mortars occurs, the over pressure induced into the pore system drives pore water out into the sample chamber and the relative humidity is abruptly increased. During the subsequent temperature decrease, ice in the mortar cavities draws the water vapor back into the pore system and the relative humidity is decreased. The lowest relative humidities in the calorimeter chambers of the wet mortar samples were measured around −55°C and the measured relative humidity values were 65–70%.
6. At the temperature at which the first freezing of the pore water occurred, the largest pressure in the pore system calculated by the theory was in test mortar M50 in which no air-entraining admixtures were applied. The calculated pore pressures were 13.4, 3.2, and 1.8 MPa for test mortars M50, M60A, and M35A,

respectively. After the first freezing, the pore pressures in the air-entrained mortars changed their sign and an under pressure prevailed until the temperature had decreased to the value of −19°C for M60A and −25°C for M35A. During thawing, the pore pressure changed to under pressure between −26 and −19°C. The lowest under pressures were calculated near 0°C, where M50 possessed a pore pressure of −16 MPa, M35A had a pore pressure of −18 MPa, and M60A obtained about −23 MPa under pressure according to the theory.

Acknowledgments

The research project was carried out during a sabbatical at Helsinki University of Technology and with financial support from Finland's Academy. The author is in debt to both of these institutions. I thank Professor Markku J. Lampinen and Dr. Seppo Matala for helpful discussions. Additional thanks are due to Dr. Matala for the use of a computer program he produced during his thesis work to calculate the heat capacity and ice evolution values from the low temperature calorimeter test results. Mr. Fahim Al Neshawy produced the test samples and performed the test runs and his help is gratefully acknowledged. I also wish to express my thanks to M. Sc. Veli-Antti Hakala and Mr. Pekka Tynnilä who helped in the building and innovation of the measuring apparatuses.

References

1. Thomson, J. *Trans. R. Soc. Edinburg* **1849,** *16*, 575–580.
2. Thomson, W. *Phil. Mag.* **1850,** *37*, 123–127.
3. Gibbs, J.W. *The Collected Works of J. Willard Gibbs, Vol. 1, Thermodynamics*; Yale University Press: New Haven, 1948.
4. Kubelka, P. *Zeitschrift für Electrochemie* **1932,** *38*, 611.
5. Powers, T.C. *J. Amer. Concr. Soc.* **1945,** *16*, 245–271.
6. Powers, T.C. *Proc. Highway Res. Board* **1949,** *33*, 28.
7. Powers, T.C.; Brownyard, T.L. *J. Amer. Concr. Inst.* **1947,** *18*, 549–602.
8. Powers, T.C.; Brownyard, T.L. *J. Amer. Concr. Inst.* **1947,** *18*, 933–969.
9. Powers, T.C.; Helmuth, R.A. *Proc. Highway Res. Board* **1953,** *32*, 285–297.
10. Everett, D.H. *Trans. Faraday Soc.* **1961,** *57*, 1541–1551.
11. Everett, D.H.; Haynes, J.M. *RILEM Bull.* **1965,** *27*, 31.
12. Litvan, C.G. *J. Colloid Interface Sci.* **1971,** *381*, 75–83.
13. Sidebottom, E.W.; Litvan, C.G. *Trans. Faraday Soc.* **1971,** *67*, 2726–2736.
14. Litvan, C.G. *J. Amer. Ceram. Soc.* **1971,** *55*, 38–42.
15. Litvan, C.G. *J. Colloid Interface Sci.* **1973,** *45*, 154–169.
16. Setzer, M.J. *Deutscher Ausschuss für Stahlbetong, Heft* **1977,** *280*, 43–117.
17. Brun, M.; Lallemand, A.; Quinson, J-F.; Eyraud, C. *Thermochim. Acta* **1977,** *21*, 59–88.
18. Atkins, P.W. *Physical Chemistry*; Oxford University Press: Oxford, 1978.
19. Penttala, V.E. *Mag. Concr. Res.* **1989,** *148*, 171–181.
20. Penttala, V.; Hannonen, P.; Järvinen, M.; Komonen, J. *Helsinki University of Technology, Department of Structural Engineering, Concrete Technology, Report 5*, 1995.
21. Hobbs, P.V. *Ice Physics*; Oxford University Press: New York, 1974.
22. Hawkes, I.; Mellor, M. *J. Glaciol.* **1972,** *61*, 103–131.